Additive Manufacturing 47 (2021) 102257

Contents lists available at ScienceDirect

Additive Manufacturing

journal homepage: www.elsevier.com/locate/addma

Surface residual stress and phase stability in unstable β-type Ti–15Mo–5Zr–3Al alloy manufactured by laser and electron beam powder bed fusion technologies

Aya Takase [a,b,*], Takuya Ishimoto [b,c], Ryoya Suganuma [b], Takayoshi Nakano [b,c,**]

[a] Rigaku Americas Corporation, 9009 New Trails Drive, The Woodlands, TX 77381, USA
[b] Division of Materials and Manufacturing Science, Graduate School of Engineering, Osaka University, 2–1, Yamadaoka, Suita, Osaka 565–0871, Japan
[c] Anisotropic Design & Additive Manufacturing Research Center, Osaka University, 2–1 Yamadaoka, Suita 565–0871, Japan

ARTICLE INFO

Keywords:
Titanium alloys
Residual stress
Phase stability
Powder bed fusion
Thermal history

ABSTRACT

The differences between the physicochemical properties of the laser and electron beam powder bed fusion (L- and EB-PBF) methods are yet to be explored further. In particular, the differences in the residual stress and phase stability of alloys with unstable phases remain unexplored. The present work is the first to systematically investigate how the heat source type and process parameters affect the surface residual stress and phase stability of an unstable β-type titanium alloy, Ti–15Mo–5Zr–3Al. The surface residual stress and β-phase behavior were studied using high-precision X-ray diffraction (HP-XRD). Significant differences were observed between the two methods. The L-PBF-made specimens exhibited tensile residual stresses of up to 400 MPa in the surface area. HP-XRD analysis revealed a stress-induced lattice distortion, interpreted as a transitional state between the β-phase and α"-phase. In contrast, the EB-PBF-made specimens showed no significant residual stress and had an undistorted β-phase coexisting with the hexagonal α-phase caused by elemental partitioning. This study provides new insights into the previously neglected effects of L-PBF and EB-PBF in unstable β-type titanium alloys.

1. Introduction

Additive manufacturing (AM) technologies have the potential to economically fabricate customized parts with complex shapes. Among the AM techniques, powder bed fusion (PBF) is suitable for fabricating small parts with complicated shapes, and their applications in biomedical implants have been widely studied [1,2]. PBF technologies use either a laser or an electron beam as the heat source, which scans a thin layer of powder and fuses pass-by-pass and layer upon layer of thin powder to build a solid part according to a computer-aided design file. These techniques are called laser powder bed fusion (L-PBF) or electron beam powder bed fusion (EB-PBF) methods, depending on the heat source. Both methods are among the few AM techniques established for industrial applications of metal AM [3,4]. L-PBF is preferred for small parts with complicated shapes, whereas EB-PBF is more suitable for larger parts for several reasons. The small surface roughness of L-PBF helps to maintain the accuracy of the shape of small parts, while its high residual stress can cause a significant deformation when fabricating larger parts. Meanwhile, EB-PBF is more suitable for larger parts owing to its lower residual stress and higher scanning speed [5].

However, despite the considerable advantages of PBF, parts produced with this technology can suffer from various defects, such as residual stress, porosity, and surface roughness. Residual stress is detrimental for the final products because it can cause deformation [6–14], initiate or accelerate crack propagation [6,13,15], and reduce the overall mechanical strength of the fabricated parts [14,16–18]. The residual stress in the surface area is particularly important to understand because cracks often start on the surface [15,19]. Phase stability is equally important to understand because when an unstable phase is used, phase change can affect the mechanical properties of the parts. The thermal history of the parts experienced during the fabrication process can be significantly different between L-PBF and EB-PBF. In the case of titanium alloys with many elements and possible polymorphs involved, this difference in thermal history can significantly influence the residual

* Corresponding author at: Rigaku Americas Corporation, 9009 New Trails Drive, The Woodlands, TX 77381, USA.
** Corresponding author at: Division of Materials and Manufacturing Science, Graduate School of Engineering, Osaka University, 2–1, Yamadaoka, Suita, Osaka 565–0871, Japan.
E-mail addresses: aya.takase@rigaku.com (A. Takase), nakano@mat.eng.osaka-u.ac.jp (T. Nakano).

https://doi.org/10.1016/j.addma.2021.102257
Received 18 April 2021; Received in revised form 18 July 2021; Accepted 14 August 2021
Available online 18 August 2021

stress, phase stability, and ultimately, the performance of the parts. Both L-PBF and EB-PBF use similar fabrication processes. Nevertheless, there are significant differences that can lead to different amounts of residual stress in the resulting parts. When fabricating an unstable phase such as β-type titanium alloys, these differences can also affect the β-phase stability and result in different crystalline phases. L-PBF typically uses a powder size of approximately 10–60 μm, whereas EB-PBF uses a coarser powder of approximately 60–105 μm [3,5]. The powder bed was preheated for EB-PBF up to several hundred degrees, typically around 500 °C for β-type titanium alloys [20,21], while preheating at a temperature commonly below 200 °C was occasionally applied for L-PBF [21]. EB-PBF is conducted in vacuum and L-PBF in Ar gas. These differences translate into different thermal histories, that is, temperature gradients, solidification rate, and the resultant cooling rates represented by the product of both. The cooling rate of L-PBF is an order of magnitude higher than that of EB-PBF with the commonly used process parameters for Ti alloys [5]. These differences in the thermal history influence the level of residual stress, β-phase stability, and the size of the microstructural features.

One of the most promising candidates for biomedical implants is β-type Ti–15Mo–5Zr–3Al owing to its biocompatibility and uniquely low Young's modulus [22,23]. The Young's modulus of β-phase Ti–15Mo–5Zr–3Al is 84.3 GPa in the polycrystalline state [23], which is a better match to that of bones (10–30 GPa) compared to 114 GPa of α-type Ti–6Al–4V. This unique property is related to the body-centered cubic (bcc) structure. However, the amount of β-stabilizing elements needs to be limited to lower its Young's modulus, making it challenging to maintain the bcc β-phase [24]. Ti–15Mo–5Zr–3Al is one such alloy with a low Young's modulus and difficulty in maintaining a single-phase. The single-phase state of the β-phase in the L-PBF and EB-PBF-fabricated Ti–15Mo–5Zr–3Al parts can be easily disturbed not only directly by the thermal history during the fabrication process, but also indirectly by a change in elemental composition or residual stress caused by the different thermal histories unique to each technique.

Although there have been comparative studies of L-PBF and EB-PBF [16,25], they focus on the differences in the mechanical properties of stable α-type titanium alloys. No in-depth comparison of the residual stress and phase stability of unstable β-type titanium alloys has been reported and is yet to be explored and understood to improve the performance of these alloys.

There are several methods for measuring residual stress [7,26–33]. Among them, the XRD method is widely used because it is non-destructive, less expensive, and more accessible than the neutron diffraction method and has a higher resolution than the ultrasonic method [26]. The XRD method is sensitive to the surface residual stress owing to its small penetration depth of 20–40 μm for Cu Kα radiation in titanium alloys. However, it should be noted that a small penetration depth could limit the number of crystallites to be measured when the crystallite size is large and comparable to the penetration depth, and it is not suitable for probing internal residual stresses. Another advantage of the XRD method is that it does not require a stress-free standard material, which otherwise is required while it can cause an error in the neutron diffraction method [34,35]. Because of its resolution, accuracy, and sensitivity to the surface area, we used the XRD method to analyze the surface residual stress in this study.

We used whole polycrystalline XRD patterns to analyze the crystal structure on the same volume analyzed for the residual stresses. Transmission electron microscopy (TEM) is often used to study the crystal structures of PBF-made alloys. However, it is destructive, and its resolution is limited to approximately 0.5 Å [36], equivalent to 15% of a typical β-type titanium unit cell size. In contrast, XRD is remarkably sensitive to the interatomic spacing change because a large volume contributes to the diffraction phenomena. We used XRD in this study for two reasons: One reason was to capture small changes in the crystal structure, which can occur before a complete phase transition. The other reason was to non-destructively measure both changes in the crystal structure and levels of residual stress on the same volume under the same measurement conditions. Furthermore, in this study, we used high-precision XRD (HP-XRD) to investigate small changes in the unstable β-phase crystalline structure that cannot be observed by conventional techniques, such as TEM. HP-XRD combines parallel beam geometry, the whole pattern fitting (WPF) method, and a high-precision systematic peak position correction to achieve a lattice distortion sensitivity of 0.02% [37,38].

This study aims to understand the influence of L-PBF and EB-PBF on the surface residual stress and phase stability of an unstable β-type titanium alloy. We fabricated Ti–15Mo–5Zr–3Al (mass %) parts using L-PBF and EB-PBF. The fabrication began with powders produced from the same ingot. The dimensions of the parts and analyzed volumes were kept the same to isolate the influences of the fabrication methods. We quantified the surface residual stresses and analyzed the changes in crystal structures in detail using HP-XRD. A systematic and quantitative comparison of the differences between the two techniques and different process parameters is reported. Furthermore, the origins of the differences and their implications for the design of PBF-made implants are discussed.

2. Material and methods

An ingot with a nominal composition of Ti–15Mo–5Zr–3Al was used as the starting material. Both powders for L-PBF and EB-PBF were produced from the same starting material by Ar gas atomization using an induction coil to melt the ingot (OSAKA Titanium Technologies, Japan). The obtained powder was spherical in shape. The particle sizes were measured using a Mastersizer 3000E particle size analyzer (Malvern Panalytical, UK). The particle sizes were D10 = 19.0 μm, D50 = 31.6 μm, D90 = 50.3 μm, and D10 = 52.1 μm, D50 = 75.5 μm, D90 = 110 μm for L-PBF and EB-PBF, respectively. Specimens with dimensions of 5 mm (width) × 5 mm (depth) × 50 mm (height) were fabricated. A total of 24 specimens of the same dimensions arranged in five-piece by five-piece grid with one vacant position at the center were fabricated at the same time. The samples measured by XRD in this study were selected from the peripheral region of the 5 × 5 square grid to minimize the effect of heat accumulation on the base plate [39]. The specimen surface was blown with compressed air to remove partially melted powder particles from the sample surface. Fig. 1 shows scanning electron microscopy (SEM) images of the powders and the appearance of the built specimens. In both L-PBF and EB-PBF, the same scan strategy in which beams were scanned parallel to the X-axis in alternating directions (Fig. 1(c)) [40,41] was employed. A contour scan was not performed. Although changing the scan direction from layer to layer can also affect the residual stress, to avoid overcomplicating the comparison of various effects such as scan direction, scan path length, related thermal history, and gas flow direction on the residual stress and crystal structure, we focused on the scan strategy without rotation in this study. For L-PBF, we used an EOS M 290 (EOS, Germany) equipped with a Yb fiber laser. The baseplate was preheated to 80 °C. Two beam conditions of beam power and scan speed at 360 W, 1200 mm/s and 75 W, 250 mm/s, were compared. Hereafter, we refer to these specimens as L-PBF-360 W and L-PBF-75 W, respectively. The hatch distance and layer thickness were 0.1 mm and 0.06 mm, respectively. For EB-PBF, we used an Arcam Q10 (Arcam, Sweden). The powder bed was preheated at 520 °C and two beam conditions of beam current and scan speed at 15 mA, 5000 mm/s and 12.5 mA, 6000 mm/s were compared. We refer to these specimens as EB-PBF-15 mA and EB-PBF-12.5 mA hereafter. The hatch distance and layer thickness were 0.1 mm and 0.05 mm, respectively. Both L-PBF and EB-PBF beam powers and scan speeds were selected to represent two sets of conditions that are largely different while achieving high-density parts for each PBF process determined by preliminary tests of a wide range of parameters. Table 1 summarizes the specimen labels and scan conditions.

For the residual stress measurements, it is required that the crystal

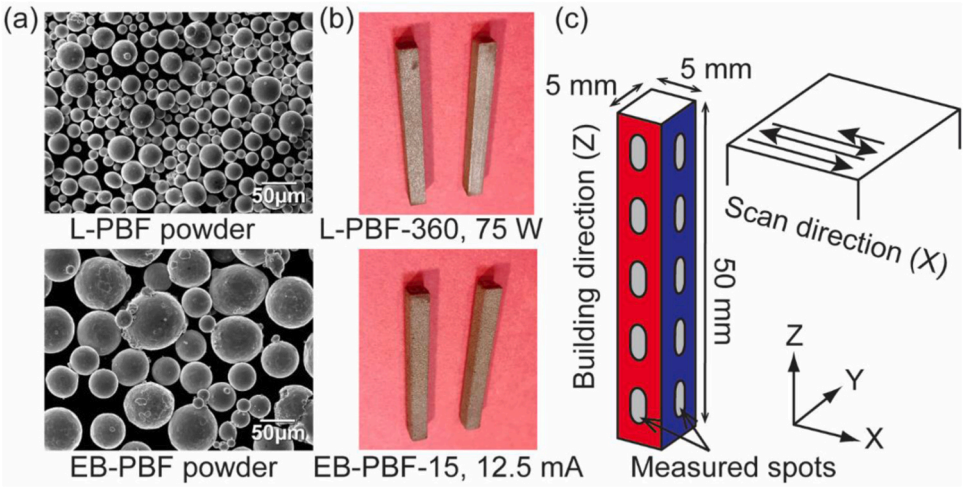

Fig. 1. (a) SEM images of gas-atomized Ti–15Mo–5Zr–3Al powders used for L-PBF and EB-PBF, (b) appearance of L-PBF- and EB-PBF-made parts, and (c) measurement locations shown with the part dimensions, coordinate axes, and the beam scan and layer building directions. Each of the "measured spots" is 4 mm long in the Z direction and 1–3 mm wide in the X or Y direction, depending on the X-ray incident angle.

Table 1
Beam conditions for L-PBF and EB-PBF.

Label	Laser beam power [W]	Scan speed [mm/s]	Hatch distance [mm]	Layer thickness [mm]
L-PBF-360 W	360	1200	0.1	0.06
L-PBF-75 W	75	250	0.1	0.06
Label	**Electron beam current [mA]**	**Scan speed [mm/s]**	**Hatch distance [mm]**	**Layer thickness [mm]**
EB-PBF-15 mA	15	5000	0.1	0.05
EB-PBF-12.5 mA	12.5	6000	0.1	0.05

grains are sufficiently small and there is no specific crystallographic orientation within the measurement volume (20–40 μm depth from surface). Prior to the measurements, we confirmed that the vicinity of the sample surface meets these requirements (see Supplementary Materials A: Fig. A1). The residual stress data and whole polycrystalline diffraction patterns were collected using a SmartLab diffractometer (Rigaku Corporation, Japan) equipped with a Cu target 9 kW rotating anode X-ray generator, a horizontal goniometer, an Eulerian cradle, an XY mapping stage, and a Si strip detector. A parabolic multilayer mirror with 0.04° beam divergence on the incident side and a parallel slit analyzer with a 0.5° acceptance angle on the receiving side achieved a parallel beam geometry with Cu Kα radiation. The X-ray generator was operated at 45 kV and 200 mA, and a Si strip detector was used as the point detector. To map the change in the residual stress and crystal structure along the building direction of the specimens, we shaped the incident X-ray beam to a 1 × 2 mm rectangle, which resulted in a beam footprint on the specimen surface of 1–3 mm wide, depending on the X-ray incident angle, and 4 mm long in the building direction. The specimen was placed such that the building direction was perpendicular to the diffraction plane defined by the incident and diffracted X-ray beams (see Supplementary Materials B: Fig. B1). To keep the analyzed volume the same between the residual stress and the crystal structure analysis, we used the same experimental setup to analyze the residual stress, identify and quantify the crystalline phases, and refine the lattice parameters.

For the residual stress measurements, we aligned and tested the diffractometer according to the ASTM E915-10 standards [42]. The residual stress measurement conditions were selected according to SAE International standards [28]. The $\sin^2\psi$ iso-inclination method was used to measure the horizontal σ_X and σ_Y components of the residual stress in the XZ and YZ planes, respectively. The $\sin^2\psi$ side-inclination method was used to measure the vertical σ_Z component of the stress in the XZ and YZ planes (see Supplementary Materials B: Fig. B2). Because the focus of this study was the surface residual stresses that can initiate cracks or reduce the mechanical strength of the fabricated parts, the residual stresses were measured after the specimens had been removed from the base plate. Therefore, the results of this XRD measurement represent the residual stresses that remained after the base plate removal. The residual stresses generally change when a part is removed from the baseplate, depending on the shape and dimensions of the parts [44]. A diffraction peak as close to 165° as possible and a sufficient number of ψ positions (seven or more) are recommended for an accurate determination of the residual stress [42]. We used the β-phase (3 2 1) reflection at approximately 124.0° and 11 points of ψ from 0.0° to 50.8° for the iso-inclination method and from 0.0° to 45.0° for the side-inclination method. At this setting, the penetration depth of the Cu Kα radiation, defined as the point where only 1% of the incident beam can travel, varied from 10 μm at side-inclination $\psi = 50.8°$ to 43 μm at $\psi = 0°$. The Young's modulus of 84.3 MPa [23] and Poisson's ratio of 0.33 were used for the residual stress calculation. The average deviation of the eleven ψ positions from the linear fit of the $\sin^2\psi$ plot was used as the size of the error bar of each residual stress value because this value reflects the validity of the linear fit model as well as the accuracy of the measurement of the diffraction angles [42]. This average deviation also indicates the detection limit of a particular measurement. We considered double this value as the detection limit for each measurement.

The whole polycrystalline diffraction patterns were analyzed using the whole pattern fitting (WPF) method to verify the single-phase state of the β-phase or to quantify the deviation from that state. A polycrystalline diffraction pattern can be calculated using the X-ray intensity I_{cal} as a function of the scattering angle 2θ using the following equation:

$$I_{cal}(2\theta) = A(2\theta)\sum_n S_n \sum_{hkl} M_{n,hkl} L_{n,hkl} I_{n,hkl} \Phi_n\left(2\theta - 2\theta_{n,hkl} - T(2\theta)\right) + y_b(2\theta), \quad (1)$$

where $A(2\theta)$ is the absorption factor and S_n is the scale factor of the nth phase. $M_{n,hkl}$, $L_{n,hkl}$, and $I_{n,hkl}$ are the multiplicity factor, Lorentz polarization factor, and integrated diffraction intensity of the (h k l) reflection of the nth phase, respectively. Φ_n is the profile shape function of the nth phase, $2\theta_{n,hkl}$ is the diffraction angle of the (h k l) reflection of the nth phase, calculated from the lattice parameters, $T(2\theta)$ is the systematic diffraction peak shift, and $y_b(2\theta)$ is the background scattering. The WPF method, also called the Pawley method when $I_{n,hkl}$ is not constrained by the crystal structure, increases the precision of the lattice parameter analysis by introducing constraints based on the crystal symmetry and profile shape function Φ_n determined by the standard reference material [43].

In addition to using the WPF method, it is essential to correct the systematic diffraction peak shifts, $T(2\theta)$ in Eq. (1), to accurately analyze the lattice parameters and quantitatively study a subtle change in the crystal structure. With the commonly used Bragg-Brentano geometry, the systematic peak shift correction requires the sample surface to be smooth and flat in the order of micrometers and a standard material with a known lattice parameter to be mixed into the specimen. However, these conditions are not achievable with PBF-made specimens because they inevitably have surface irregularities based on the difference in powder particle size used. In contrast, the parallel beam geometry does not have specimen-specific systematic peak shifts or surface roughness and curvature-related peak shifts. Therefore, all peak shifts are independent of the specimen and its surface condition, and they can be fully corrected using a standard reference material measured separately from the specimen. The peak shift $T(2\theta)$ in Eq. (1) can be modeled using the following equation:

$$T(2\theta) = P_1 + \frac{P_2}{\tan 2\theta} + P_3 \cos\theta. \tag{2}$$

where P_1, P_2, and P_3 are the fitting parameters. These parameters were refined in the WPF analysis of the standard reference material, while the lattice parameter was fixed at a certified value. The refined P_1, P_2, and P_3 were then fixed to correct the systematic peak shifts, and the lattice parameters of Ti–15Mo–5Zr–3Al were refined by fitting the entire diffraction pattern using Eq. (1). By combining the parallel beam geometry, systematic peak shift correction, and WPF method, the HP-XRD method can analyze lattice parameters with a sensitivity of 0.02% or better [37,38].

We also used the WPF method to quantify the mass percentage of each phase. The WPF method can introduce constraints in diffraction peak intensities by theoretically calculating the integrated diffraction intensity, $I_{n,hkl}$ in Eq. (1), based on the atomic coordinates. This technique is called the Rietveld method. When the diffraction peak intensity constraints are introduced, the scale factor, S_n, in Eq. (1), can be converted into the mass % of the nth phase in a mixture [45].

In this study, we used HP-XRD to analyze the lattice parameters and the quantity of each Ti–15Mo–5Zr–3Al phase. We used the split pseudo-Voigt function as the profile shape and constrained the diffraction peak shape and width as a function of the diffraction angle. The systematic diffraction peak shifts were corrected to remove the errors in the lattice parameter analysis by measuring a standard reference lanthanum hexaboride powder, NIST SRM 660c (National Institute of Standard and Technology, USA), with a known lattice parameter of 4.156826 ± 0.00008 Å at 22.5 °C, certified by the National Institute of Standards and Technology [46]. The diffraction peak widths of NIST SRM660c were also used to correct the diffraction peak broadening caused by the finite resolution of the diffractometer and estimate the crystallite size and random lattice strain of the specimens. These factors broaden the diffraction peaks but can be analyzed separately by using multiple diffraction peaks over a wide range of diffraction angles [47].

To understand the origin of the differences in the surface residual stress and crystal structures observed on the L-PBF-made parts between different process parameters, we performed finite element analysis to simulate the heat transfer and temperature change during the L-PBF process. COMSOL Multiphysics® 5.5 (COMSOL Inc., USA) was used for the numerical simulation. The dimensions of the finite element model were 5 (width) × 5 (depth) × 2 (height) mm. In the simulation, the laser scanned the entire 5 × 5 mm XY plane to calculate the temperature distribution at the center of both the XZ and YZ planes. The L-PBF-360 W and L-PBF-75 W scanning conditions listed in Table 1 were used in the simulation. Under these conditions, the laser made 25 round trips per 60 μm thick layer. As we assume that the heat flux from the laser beam satisfies the Gaussian distribution [48–50], the three-dimensional energy distribution can be expressed as a function of radius r and depth z:

$$Q_0(r,z) = \frac{2\alpha P}{\pi R^2 z_0} exp\left(-\frac{2r^2}{R^2}\right) \times \left(1 - \frac{z}{z_0}\right) \qquad (0 < z < z_0) \tag{3}$$

where α is the heat absorptivity of the laser beam on the metal powder bed, P is the laser power, R is the radius of the beam set to 50 μm [51,52], and z_0 is the penetration depth of the laser. In this calculation, the powder bed was not modeled, but α was set to 85% to consider the high heat absorptivity of the powder bed [48]. Further, z_0 was adjusted based on the melt-pool dimensions [53,54]. The temporal and spatial heat transfer is governed by the following equation [55,56]:

$$\rho C \frac{\partial T}{\partial t} + \nabla \cdot \boldsymbol{q} = Q \tag{4}$$

where ρ is the material density, C is the specific heat capacity, T is the temperature, t is the time, $\boldsymbol{q}$ is the heat flux, and Q is the amount of heat generated per unit volume. The latent heat was considered by incorporating it into the temperature dependence of the specific heat capacity [57,58]. The heat flux due to heat conduction is represented by the following equation, according to Fourier's law:

$$\boldsymbol{q} = -k\nabla T \tag{5}$$

where k is thermal conductivity. The boundary conditions on the outer surface of the model are set using the following equation:

$$-\boldsymbol{n} \cdot \boldsymbol{q} = q_0 = h(T_{ext} - T) \tag{6}$$

where $\boldsymbol{n}$ is the normal vector of the surface through which the heat flows, h is the heat transfer coefficient and was set to 10 W/m^2 K, and T_{ext} is the external temperature at which the model contacts the environment. Table 2 lists the thermal properties used in the simulation. The material density was set to 5010 kg/m^3 [59], and the liquidus and solidus temperatures were calculated using JMatPro® Version 9.1 (Sente Software, UK).

3. Results

3.1. Residual stress analysis by the sin$^2\psi$ method

The sin$^2\psi$ plots for the residual stress in the horizontal direction σ_X at Z = 5 mm on the XZ plane, at the beginning of the growth, for L-PBF-360 W and EB-PBF-15 mA are shown in Fig. 2. The sin$^2\psi$ plot of L-PBF-360 W shows a linear correlation between sin$^2\psi$ and the diffraction

Table 2
Thermal properties used in the simulation.

Property	Value [unit]
Solidus temperature	1998 [K]
Liquidus temperature	2018 [K]
Density	5010 [kg/m^3]
Thermal conductivity of solid	21 [W/m K]
Thermal conductivity of liquid	29 [W/m K]
Specific heat capacity of solid	670 [J/kg K]
Specific heat capacity of liquid	730 [J/kg K]
Latent heat	370 [kJ/kg]

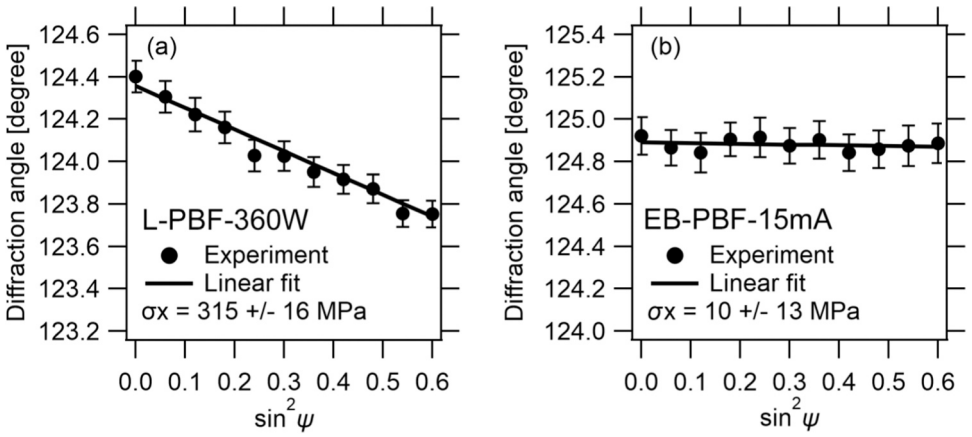

Fig. 2. $Sin^2\psi$-plots for residual stress in the horizontal direction σ_X on (a) L-PBF-360 W and (b) EB-PBF-15 mA measured on the XZ plane at Z = 5 mm.

angle with a Pearson correlation coefficient $r = -0.988$ at a tensile stress of 315 ± 16 MPa. However, the plot of EB-PBF-15 mA shows a flat line, indicating that there is no residual stress in the surface area detectable by this XRD measurement. These results experimentally demonstrated that the L-PBF-made part suffered from a large amount of residual stress, while the EB-PBF-made part did not, as previously suggested by indirect comparisons [60–62]. This experiment successfully isolated the difference between the two fabrication processes by keeping the starting material, the resulting part dimensions, and the residual stress measurement conditions the same between the two specimens.

Fig. 3 shows the residual stress values as a function of the location along the building direction Z for the L-PBF-made specimens. The XZ plane of L-PBF-360 W (Fig. 3(a)) showed the highest overall tensile residual stress of all measured planes, ranging from 146 ± 16 MPa to 402 ± 60 MPa. The residual stresses on the YZ plane (Fig. 3(b)) were lower than those of XZ and ranged from 27 ± 11 MPa to 94 ± 17 MPa. In addition, L-PBF-75 W showed residual stress ranging from less than the detection limit of this measurement to 87 ± 20 MPa on both the XZ and YZ planes (Fig. 3(c) and (d)). Overall, these values were lower than those of L-PBF-360 W. These results indicate the following: (1) The higher laser power and the higher scan speed of L-PBF-360 W, 360 W and 1200 mm/s, resulted in greater residual stress than that of L-PBF-75 W, 75 W and 250 mm/s, while the energy density was maintained at 50 $W/mm^3/s$. (2) The XZ plane parallel to the laser beam scan direction retained higher residual stresses than the YZ plane perpendicular to the scan direction.

Fig. 4 shows the residual stress values as a function of the location along the building direction for the EB-PBF-made specimens. Between EB-PBF-15 mA (Fig. 4(a) and (b)) and EB-PBF-12.5 mA (Fig. 4(c) and (d)), the residual stress values were scattered between − 37 ± 22 MPa and 75 ± 36 MPa. These can be regarded as very little to no stress, considering that the stress values are below the detection limit.

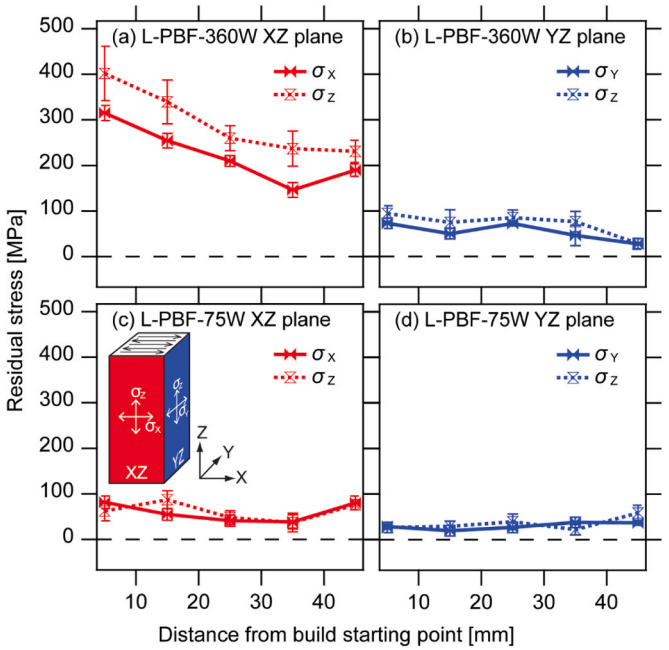

Fig. 3. Measured residual stress in the horizontal and vertical directions, σ_X, σ_Y, and σ_Z, on the (a) L-PBF-360 W XZ plane, (b) L-PBF-360 W YZ plane, (c) L-PBF-75 W XZ plane, and (d) L-PBF-75 W YZ plane at different locations along the building direction. The insert shows the measured planes and residual stress directions.

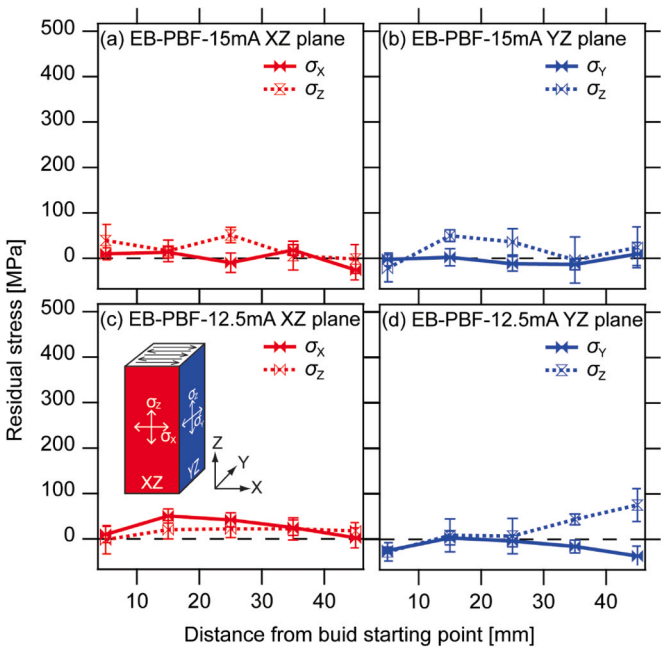

Fig. 4. Measured residual stress in the horizontal and vertical directions, σ_X, σ_Y, and σ_Z, on the (a) EB-PBF-15 mA XZ plane, (b) EB-PBF-15 mA YZ plane, (c) EB-PBF-12.5 mA XZ plane, and (d) EB-PBF-12.5 mA YZ plane at different locations along the building direction. The insert shows the measured planes and residual stress directions.

3.2. β-phase stability analysis by the Whole Pattern Fitting (WPF) method

The XRD patterns of the L-PBF raw powder, L-PBF-360 W on the XZ plane at Z = 5 mm, EB-PBF raw powder, and EB-PBF-15 mA on the XZ plane at Z = 5 mm are shown in Fig. 5(a). These XRD patterns confirm that the L-PBF raw powder and L-PBF-360 W consisted of only the β-phase, while the EB-PBF raw powder and EB-PBF-15 mA had the α-phase and β-phase. The raw powder completely melted during the EB-PBF process; thus, the α-phase in the EB-PBF raw powder did not affect the phase composition of the resulting parts. After the fabrication process, a higher amount of α-phase appeared, as seen in the XRD pattern of EB-PBF-15 mA. It is also worth noting that the β-phase diffraction peaks of the EB-PBF raw powder and EB-PBF-15 mA were broader than those of the L-PBF raw powder and L-PBF-360 W. A small crystallite size of less than 100 nm and random lattice strain can cause diffraction peak broadening [63]. The random lattice strain, representing the degree of lattice disorder in percentage, was estimated for the β-phase using WPF. The random lattice strain values were 0.227 ± 0.009% for the L-PBF powder and 0.43 ± 0.01% for the EB-PBF powder. No effect of small crystallite size was observed in the raw powders. For EB-PBF-15 mA, the crystallite size and random lattice strain for the β-phase were estimated to be 26 ± 2 nm and 0.51 ± 0.011%, respectively. The crystallite size estimated here is defined as the size of a single crystal that coherently diffracts X-rays, and it is different and can be much smaller than the grain size observed optically or by SEM.

Fig. 5(b) shows the XRD profiles of the L-PBF powder and L-PBF-360 W (XZ plane, Z = 5 mm) around the β-phase (3 1 0) reflection. The (3 1 0) reflection of L-PBF-360 W splits into multiple peaks, while the same reflection of the L-PBF powder is a single peak. This peak split indicates that the bcc structure in the L-PBF-made specimen was distorted and became a body-centered tetragonal (bct) structure, as previously reported by the authors [64]. We assumed a bct structure with c slightly shorter than a and applied the WPF analysis. The bcc phase peaks can overlap with the bct peaks; thus, we cannot identify whether the bct and bcc phases co-exist. To limit the degrees of freedom, we assumed a single-phase bct. This bct structure model fits the observed diffraction pattern well, and the goodness of fit parameter R_{wp} decreased from 13.93% for the bcc model to 10.84%. A smaller R_{wp} value indicates a better fit. As a result of the WPF analysis, the L-PBF-360 W lattice parameters were refined as $a = 3.2684 \pm 0.00014$ Å and $c = 3.2426 \pm 0.00025$ Å, exhibiting a 0.79% difference between the two axes. The diffraction pattern of the L-PBF raw powder did not show any peak split and was fitted by assuming a bcc structure. The lattice parameter was refined to $a = 3.2647 \pm 0.0002$ Å (see Supplementary Materials C: Fig. C(a) and C(b) for the WPF analysis results).

The lattice parameters were analyzed using the Pawley method for L-PBF-360 W and L-PBF-75 W at all locations, as shown in Fig. 1(c). Fig. 6 shows the refined lattice parameters as a function of the distance from the growth starting point. The lattice parameter of the L-PBF raw powder, 3.2647 ± 0.0002 Å, is shown as a reference value determined

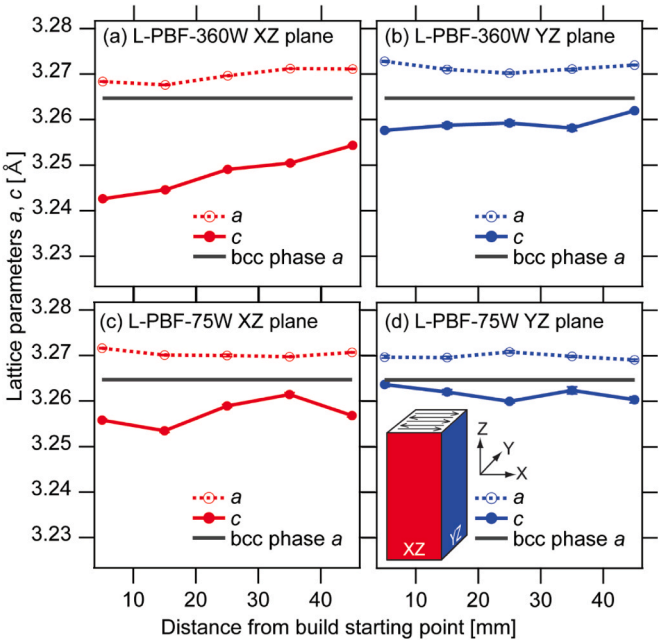

Fig. 6. Refined lattice parameters a and c of the bct β-phase on the (a) L-PBF-360 W XZ plane, (b) L-PBF-360 W YZ plane, (c) L-PBF-75 W XZ plane, and (d) L-PBF-75 W YZ plane at different locations along the building direction. The gray line shows the bcc structure lattice parameter obtained from L-PBF raw powder as a reference. The insert shows the measured planes.

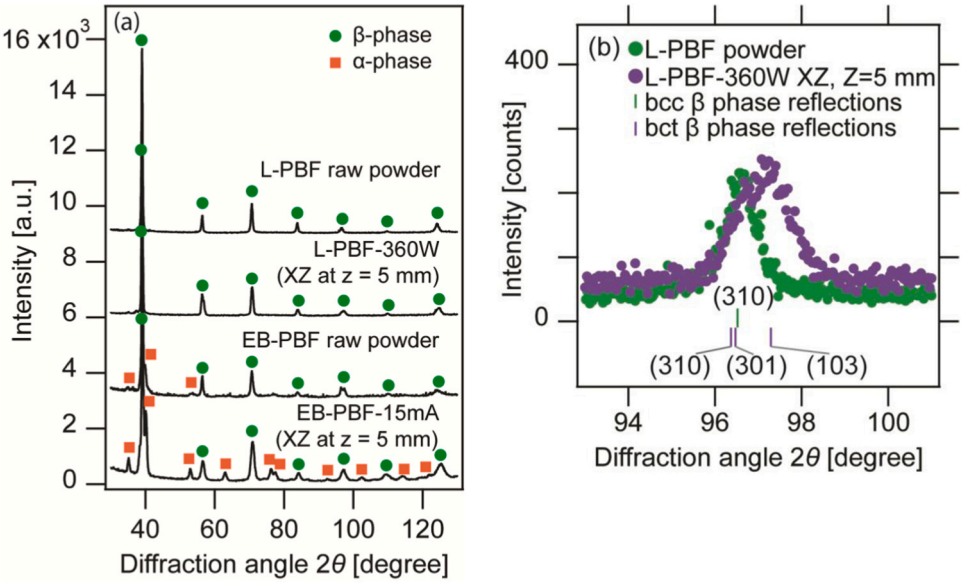

Fig. 5. (a) Whole polycrystalline XRD patterns of L-PBF raw powder, L-PBF-360 W on the XZ plane at Z = 5 mm, EB-PBF raw powder, and EB-PBF-15 mA on the XZ plane at Z = 5 mm. The α- and β- phase peaks are labeled. (b) The XRD patterns of L-PBF raw powder and L-PBF-360 W on the XZ plane at Z = 5 mm around the bcc (3 1 0) reflection. The L-PBF-360 W peak is splitting into the bct (3 1 0), (3 0 1), and (1 0 3) reflections.

for a residual-stress-free and single-bcc-phase Ti–15Mo–5Zr–3Al. The XZ planes (Fig. 6(a) and (c)) showed a more significant difference between *a* and *c*, which translates to a greater deviation from the bcc structure compared to the YZ planes (Fig. 6(b) and (d)). Additionally, L-PBF-360 W showed a greater deviation from the bcc structure than L-PBF-75 W. These results indicate that the higher laser beam power, scanning speed, and continuous beam scan in one direction are responsible for the deviation from the bcc structure. It should be noted that these lattice parameters were measured using lattice planes parallel to the specimen surface. The spacing of these lattice planes decreased as the tensile residual stress value of the same location increased. The residual stress affects all the (*h k l*) lattice planes parallel to the measured surface. Therefore, when the crystals are randomly oriented, all crystallographic axes shrink because of the tensile stress. This means that all (*h k l*) reflections observed in the whole XRD pattern in this study were equally affected by the stress, and all diffraction peaks shifted to the positive side. However, these peaks do not split because of the overall strain directly caused by residual stress. The (*h k l*)-dependent peak split is only caused by a lowered symmetry, that is, a deviation from the bcc to bct structure, involving expanding the *a* and *b* axes and shrinking the *c* axis selectively, regardless of their grain orientation, instead of shrinking all axes [64].

The β-phase lattice parameter and the ratio of β- and α-phases were analyzed using the Rietveld method for EB-PBF-15 mA and EB-PBF-12.5 mA at all locations, as shown in Fig. 1(c). To refine the ratio of the β- and α-phases, we maintained the relative peak intensity restrained by each structure's atomic coordinates. Fig. 7(a) shows the refined β-phase lattice parameters as a function of the distance from the growth starting point. In contrast to the L-PBF-made specimens, the EB-PBF-made specimens showed no peak split caused by a change in the crystal structure symmetry, indicating that the β-phase remained bcc. Furthermore, no notable difference was observed between the XZ and YZ planes or between EB-PBF-15 mA and EB-PBF-12.5 mA. On both planes of both specimens, however, the bcc β-phase lattice parameter increased along the building direction. As shown in Fig. 7(a), at the beginning of the growth, the β-phase lattice parameters of the EB-PBF-made specimens were shorter than those of the reference values obtained from the residual-stress-free and single-bcc-phase raw powders. The β-phase lattice parameters increased toward the reference value as the specimens grew, although there was no significant amount of residual stress that changed the lattice spacing. This trend indicates that there is another factor, such as a shift in the elemental composition, at play that changes the lattice parameter.

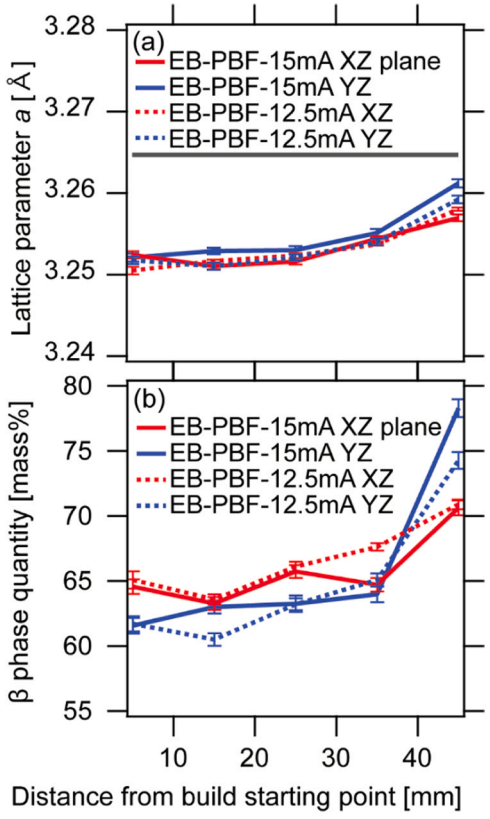

Fig. 7. (a) Refined lattice parameters and (b) mass% of the bcc β-phase of the EB-PBF-15 mA XZ plane (red solid line), EB-PBF-15 mA YZ plane (blue solid line), EB-PBF-12.5 mA XZ plane (red dashed line), and EB-PBF-12.5 mA YZ plane (blue dashed line) at different locations along the building direction. The gray line in (a) shows the bcc structure lattice parameter obtained from L-PBF raw powder as a reference.

Fig. 7(b) shows the mass percentage of the β-phase as a function of the distance from the growth starting point. It ranged from 60.5 ± 0.5 mass% to 78.3 ± 0.7 mass% and increased along the building direction. No notable difference was observed between the XZ and YZ planes or between EB-PBF-15 mA and EB-PBF-12.5 mA. The lattice parameter of the β-phase decreased as the amount of the α-phase increased. This correlation indicates that elemental exchange between the α- and β-phases simultaneously changes the β-phase lattice parameter and the α- and β-phase ratio.

3.3. Elemental composition analysis by SEM-EDS

To investigate the mass% of each element in the α- and β-phases, we applied scanning electron microscopy energy-dispersive X-ray spectroscopy (SEM-EDS) and electron backscattering diffraction (EBSD) to the near-surface area of the EB-PBF-15 mA XZ plane at Z = 25 mm. Fig. 8(a) and (b) show the SEM and EBSD results, respectively. Fig. 8(c) and (d) shows the EDS maps of Mo and Ti, respectively, in the same area. The estimated penetration depth of the electron beam of 10 kV, the setting used in this experiment, is estimated to 0.63 μm [65,66]. The finite penetration depth can reduce the spatial resolution of the experiment and affect the accuracy of the absolute values of the EDS analysis. However, the majority of the EDS analysis results come from the center area of the electron beam [67]. Furthermore, the EBSD result in Fig. 8(b) indicates that the spatial resolution of this experiment was sufficient to differentiate between the α- and β-phases. Therefore, the relative discrepancy in the chemical composition between the α- and β-phases observed in the EDS measurements shown in Fig. 8(c) and (d) is meaningful. The EDS map of Mo shows a smaller amount of Mo in the α-phase compared to that in the β-phase. The mass% of Ti, Mo, Zr, and Al were analyzed at three locations for each phase and averaged. The results are shown in Table 3. Mo and Ti showed an approximately 4 mass% difference between the α- and β-phases with Mo partitioning to the β-phase. Al showed a slight difference, partitioning toward the α-phase. Zr did not exhibit significant partitioning. These results demonstrate that the β-stabilizing element, Mo, partitioned to the β-phase, mainly replaced Ti, and made the β-phase Mo-rich and more β-stable while leaving the α-phase Mo-poor and more α stable.

4. Discussion

4.1. Validity of the XRD residual stress analysis

Because residual stress analysis methods are often based on multiple assumptions, we now discuss the validity of the assumptions of the $\sin^2\psi$ method in the present study. The residual stress σ in the direction perpendicular to the rotation axis of the ψ angle is calculated from the following equation in the $\sin^2\psi$ residual stress analysis method [28]:

$$\sigma = -\frac{E}{2(1+\nu)} \cdot \cot\theta_0 \cdot \frac{\Delta 2\theta}{\Delta(\sin^2\psi)} \tag{7}$$

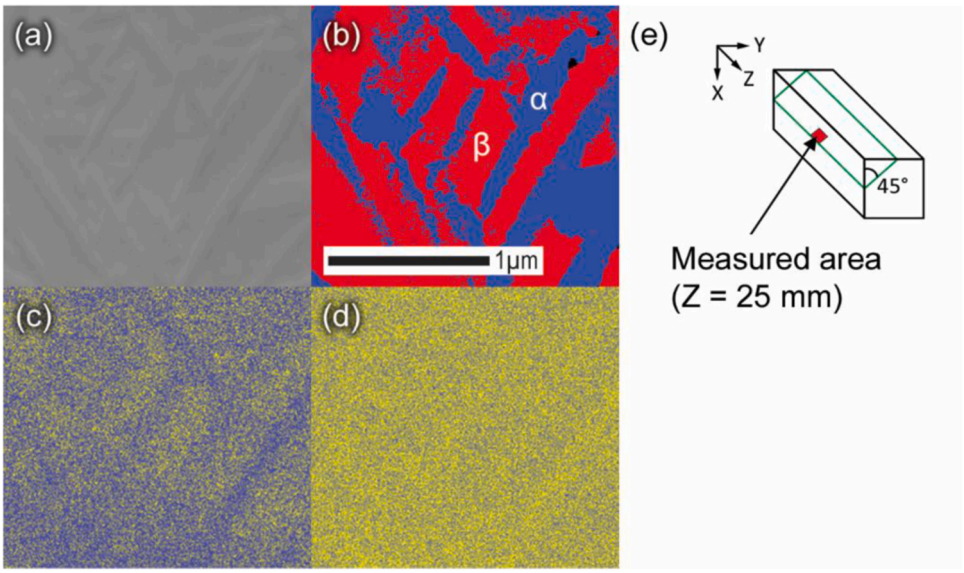

Fig. 8. (a) SEM, (b) EBSD, (c) EDS map of Mo, and (d) EDS map of Ti at the near-surface region of EB-PBF-15 mA XZ plane at Z = 25 mm. Yellow and blue indicate high and low concentrations, respectively. The results show that the β-phase is Mo-rich, and the α-phase is Mo-poor. (e) Schematic of the measured location.

Table 3
Elemental compositions of α- and β-phases determined by SEM-EDS (The near-surface region of EB-PBF-15 mA XZ plane at Z = 25 mm).

Phases	α	β
Ti	77.3 ± 1.0	73.3 ± 0.6
Mo	14.6 ± 0.8	18.9 ± 0.5
Zr	5.4 ± 0.3	5.4 ± 0.2
Al	2.7 ± 0.1	2.4 ± 0.1

where E is Young's modulus, ν is Poisson's ratio, and θ_0 is half the diffraction angle of a material with no residual stress. First, we assume that a known diffraction angle taken from a commonly used database such as the International Center for Diffraction Data (ICDD) or measured from a powder specimen is the same as the θ_0 value of the measured specimen with the residual stress removed. This is a valid approximation because the effect of a small lattice parameter change on the value cot θ_0 is negligible, especially when the diffraction angle is high. Furthermore, note that cot θ_0 is a scale factor; therefore, the error in this value might cause a slight shift in the overall stress values, but it never causes a false positive when there is no residual stress. Second, Eq. (7) is derived based on the assumption that the strains are linearly dependent on $\sin^2\psi$. This assumption is invalid when the relationship is not linearly dependent, which could occur when there is shear stress out of the plane on the surface, large crystallite size, preferred crystallographic orientation, or high strain gradient in the analyzed region. The linearity of the $\sin^2\psi$ plot shown in Fig. 2(a) ensures that none of these factors exist in the specimens analyzed in this study. Hence, we can conclude that the second assumption of this analysis method is valid.

4.2. Residual stresses in L-PBF-made specimens

The residual stresses of the L-PBF-made specimens were dependent on the process parameters, the distance from the growth starting point, and the relationship to the beam scan direction, as shown in Fig. 3. All of these parameters are related to the different local temperature gradients and cooling rates around the molten area. First, we discuss the relationship between the residual stress and the distance from the growth starting point. The residual stress of L-PBF-360 W gradually decreased as the specimen grew in the Z direction on both the XZ and YZ planes, while L-PBF-75 W showed a minimal amount of residual stress with no significant change in the building direction. At the beginning of the growth process, the heat generated by the laser beam immediately escapes to the base plate, and the overall growth layer temperature drops rapidly [68,69]. As the specimens become taller or thicker, it takes longer for the heat to escape to the base plate because more heat starts to dissipate from the specimen surface to the atmosphere, which is a slower cooling process. At the same time, the rapid temperature change and greater temperature gradient are the leading causes of residual stress in metal parts produced by AM [2,14,18,71,72]. Therefore, we can understand the gradual decrease in the residual stress of L-PBF-360 W as follows. As the specimen grew, the cooling process slowed down, the local temperature gradient decreased, and those changes along the building direction resulted in a reduction in residual stress.

Next, we discuss the difference in residual stress between the XZ and YZ planes. This difference arises from the difference in the directions of the planes relative to the beam scan direction. The XZ plane is parallel to the laser beam scan direction and shows a higher level of residual stress (Fig. 3(a) and (c)) than the YZ plane perpendicular to the beam scan direction (Fig. 3(b) and (d)). These trends were the same for both L-PBF-360 W and L-PBF-75 W, with L-PBF-360 W showing a more significant difference. A difference in the residual stress between the parallel and perpendicular directions to the beam scan direction has been previously reported [7,73]. However, these studies were conducted on the surface of a thin plate-shaped specimen. The residual stress anisotropy observed in this study was on the side planes of a tall specimen as opposed to the scanned surface, and it requires a different explanation.

Because the laser beam scan was always in the X direction, the XZ and YZ planes experienced different temperature gradients. On the XZ plane, as shown in Fig. 9(a), the laser beam moves in one direction, and the molten area starts cooling immediately after the laser beam passes. In contrast, the laser beam makes a U-turn on the YZ plane and starts scanning the next line on the same side that was just scanned. This U-turn motion results in the laser beam scanning two lines only 0.1 mm apart right after another and slows down the cooling process. To determine the temperature, heating, and cooling rate differences between the XZ and YZ planes, we simulated the temperature at the center of the XZ and YZ planes for four different depths, starting from the top XY surface scanned by the laser beam to a depth of 240 μm with a 60 μm interval. The point of calculation was set at a 20 μm depth from the XZ and YZ planes, to represent the area analyzed using XRD. The L-PBF-360 W conditions, 360 W and 1200 mm/s, were used for the simulation. The

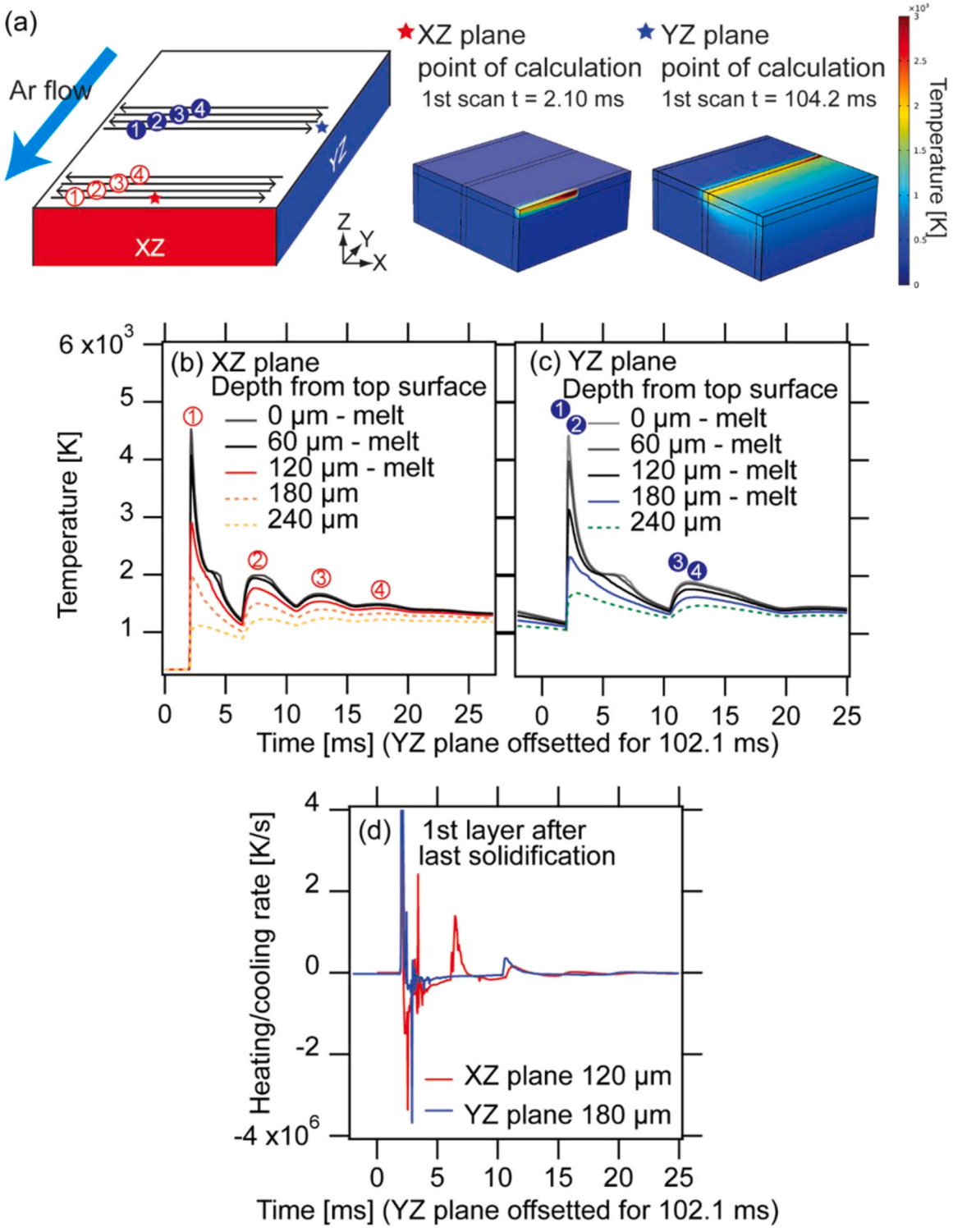

Fig. 9. (a) Schematic diagrams of laser scan strategy, the points of calculation, and simulated temperature when the point of calculation is scanned for the first time on the XZ and YZ planes. The point of simulation is 20 μm deep from the XZ and YZ planes. (b) and (c) show the temperatures calculated on those points from the 1st to 4th layers (0–240 μm from the XY plane at a 60 μm step). (d) shows the heating and cooling rate comparison between the XZ and YZ planes for the 1st scan after the last solidification process. The process parameters of L-PBF-360 W were used for the simulation.

simulated temperatures are shown in Fig. 9(b) and (c). The scan numbers in Fig. 9(a) are marked on the simulation results to indicate the scan that causes each temperature peak. The time axis for the YZ plane is offset by 102.1 ms to compensate for the time required for the laser beam to reach the center of the YZ plane. Fig. 9(c) shows that scans ❶ and ❷ do not have enough time to cause a temperature decrease between the two scans, so the temperature peaks caused by those two scans form one broad peak. The same process was repeated for scans ❸ and ❹. On the XZ plane, the equivalent four scans ①—④ have a 4.16 ms interval and form four distinctive peaks. The heating and cooling rate the part experiences after the alloy completely solidifies the last time dictates the level of residual stress. Thus, we focused on the heating and

cooling rates of the first layer after the temperature reached the solidus temperature of Ti–15Mo–5Zr–3Al, 1998 K (1725 °C), for the last time. Fig. 9(d) shows a comparison between the XZ and YZ planes. This comparison shows that the XZ plane experiences greater heating and cooling rates than the YZ plane. This difference translates to more significant local temperature gradients on the XZ plane and explains its higher residual stress levels compared to that of the YZ plane. This difference in the residual stress level between the XZ and YZ planes suggests that changing the beam scan direction from layer to layer can be an effective way to manipulate the residual stress.

Another possible cause of the difference between the XZ and YZ planes is the relationship with the Ar gas flow. The Ar gas can also affect the residual stress, as previously reported by Mishurova et al. [68] on L-PBF-made parts with dimensions similar to those of the parts studied here. Reijonen et al. [70] also reported that reducing the gas flow rate by half can reduce the melt pool size by as much as 50%, indicating the significant influence of the gas flow rate on the thermal history. As indicated in Fig. 9(a), the Ar gas flow was in the negative Y direction, which was perpendicular to the XZ plane. When the laser beam makes a U-turn on the YZ plane, the Ar gas carries the heat from the molten area toward the area that was just scanned and keeps the previously scanned area warm longer. In contrast, on the XZ plane, the laser beam moves in the direction perpendicular to the Ar gas flow, and the gas carries the heat from the molten area only to the area that was scanned 4.16 ms ago. This difference in the relationship with the Ar gas flow direction could also contribute to the lower residual stress level on the YZ plane than that on the XZ plane.

Next, we considered the difference between L-PBF-360 W and L-PBF-75 W. Scanning a laser beam at a higher power causes the temperature of the powder to increase and decrease rapidly compared to the lower power when the scanning speed is the same. Thus, higher power results in greater residual stress compared with lower power [69]. With respect to the scanning speed, contradicting cases of higher scan speed increasing residual stress [71] and decreasing residual stress [72] have been reported. At the same time, Yadroitsev et al. [73] have observed that the laser beam power influences the molten pool temperature more than the scanning speed. These previously reported results indicate that the residual stress cannot be discussed as a simple function of the energy density, and the cooling rate and temperature gradient need to be considered. In this study, L-PBF-360 W was fabricated at a laser power (360 W) than L-PBF-75 W (75 W), while the scan speed was adjusted to keep the energy density the same at 50 W/mm^3/s. We compared the simulated heating and cooling rates at a depth of 120 μm on the XZ plane for the two sets of process parameters. The maximum heating and cooling rates caused by scanning ② at 75 W and 250 mm/s were 35.9% and 30.7% lower than those at 360 W and 1200 mm/s, respectively. These simulation results correlate well with the residual stress difference between L-PBF-75 W and L-PBF-360 W and show that an increase in the cooling rate causes an increase in the residual stress.

4.3. Reduced β-phase stability of L-PBF-made specimens

As shown in Fig. 5, the L-PBF-made parts exhibited a bct structure, which is a distorted bcc structure. This structure is similar to the face-centered orthorhombic α" phase, which occurs in β-type Ti-Nb alloys [23,74,75]. Fig. 10(a) shows a comparison of these structures. The *a*" axis of the α"-phase is shorter than *c*"/$\sqrt{2}$, and this corresponds to the *c*' axis of the bct β structure being slightly shorter than the *a*' axis. It should be noted that, in a randomly oriented polycrystalline material, the residual stress changes the lattice parameter regardless of the crystallographic orientation, but according to the direction of the residual stress. The crystallographic orientation-dependent lattice parameter change, similar to that observed in this bct β structure, is caused by a phase transformation. The space groups of the bcc β-, bct β-, and orthorhombic α"-phases are Im$\bar{3}$m, I4/mmm, and Cmcm, respectively. These structures have closely related atomic arrangements, and I4/mmm (bct β-phase) is an intermediate structure between the high-symmetry Im$\bar{3}$m (bcc β-phase) and the low-symmetry Cmcm (orthorhombic α"-phase) structures [74]. The amount of distortion of the bct β structure observed in the L-PBF-made specimens was also between those two structures. The lattice parameters *a* and *c* of the bcc β-phase are equal, while they are more than 1% different for typical orthorhombic α"-phase titanium alloys such as Ti–Nb [75]. The difference observed in the L-PBF-made specimens in this study was less than 1%. These results indicate that the bct β-phase observed in the L-PBF-made specimens might be a precursor to the fully distorted orthorhombic α"-phase.

We now discuss the origin of the lattice distortion that transformed the bcc β-phase to the bct β-phase. Both the lattice parameters of the bct β-phase and the residual stresses changed as functions of the distance from the base plate. By combining the results from both L-PBF-360 W and L-PBF-75 W, we studied the correlation between the lattice parameters and residual stress to determine whether the residual stress could be the cause of the lattice distortion. Fig. 10(b) shows the relationship between the residual stress and the deviation factor, defined as

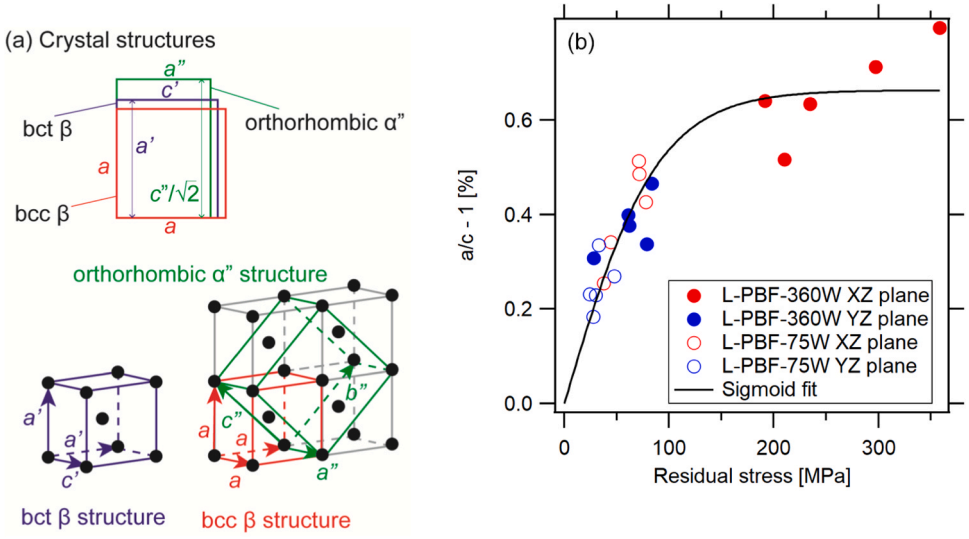

Fig. 10. (a) Relationship between the bcc β-phase, bct β-phase, and the face-centered rhombohedral α"-phase structures. (b) Deviation from bcc structure, (a/c −1) in percentage, versus the residual stress for all measurement points on L-PBF-360 W and L-PBF-75 W. The black line shows the best fit by the modified sigmoid function.

the deviation from bcc, $(a/c - 1) \times 100\%$. This factor was zero for the bcc β structure. As shown in Fig. 10(b), the deviation factor increases rapidly with a small amount of residual stress, and then saturates at approximately 0.65%. This relationship can be empirically expressed using the sigmoid function that is modified such that the deviation is zero when there is no residual stress:

$$(a/c-1) \times 100 = -\frac{1}{2}p + \frac{p}{1+\{\exp(-\sigma/q)\}} \quad (8)$$

where σ is the residual stress, and p and q are constants determined as 1.3264 ± 0.0703 and 44.363 ± 4.73, respectively, by curve fitting. To assess the strength of the correlation between the deviation factor and residual stress, we rewrite Eq. (8) as a linear function:

$$(a/c-1) \times 100 = A \times x + B \quad (9)$$

where A and B are constants, and x is a residual-stress-dependent variable defined as:

$$x = \frac{1}{1+\exp(-\sigma/q)}. \quad (10)$$

The Pearson correlation coefficient was estimated at 0.92 by fitting the x versus $(a/c - 1) \times 100$ scatter plot with the linearized Eq. (9). This result suggests a strong correlation between the residual stress and the deviation from the bcc structure.

The orthorhombic α"-phase is known to become closer to the bcc β structure as the structure gradually becomes more β-stable by alloying an increasing amount of β-stabilizing elements. This can be observed as the lattice parameters a", $b"/\sqrt{2}$, and $c"/\sqrt{2}$ become closer to the lattice parameter a of the bcc β-phase [75,76]. Furthermore, the stress-induced phase change from the bcc β- to orthorhombic α"-phase has been reported in Ti-Nb [74,75]. The previously reported results and the correlation between the residual stress and the deviation factor shown in Fig. 10(b) suggest that the residual stress disturbed the bcc β-phase stability and induced the bct β-phase. Additionally, the sigmoid function shape of the residual stress versus deviation factor plot suggests that only a small amount of residual stress is required to induce the bct β-phase, and there is no apparent threshold. It also indicates that continuing to increase the residual stress does not further deviate this structure from the bcc β-phase and induces the complete α"-phase.

4.4. Reduced β-phase stability in EB-PBF-made specimens

As Fig. 4 shows, very little to no residual stress was observed in EB-PBF-15 mA and EB-PBF-12.5 mA. This result confirms that EB-PBF-made specimens suffer little to no residual stress experimentally, as previously suggested [60–62]. All EB-PBF-made specimens maintained the bcc β-phase, which further indicates that the bct β-phase in the L-PBF-made specimens was induced by the residual stress.

Although the β-phase remained bcc in the EB-PBF-made specimens, its lattice parameter was shorter than that of the reference powder specimen by 0.33% on average, as shown in Fig. 7(a). The Mo partitioning to the β-phase observed in Fig. 8 can cause this reduction of the lattice parameter. Huang et al. [77] showed by simulation that β stabilizing solutes with $e/a = 6$–9 can distort the nearest-neighbor bonds and reduce the bond length significantly. Mo with $e/a = 6$ can reduce the bond length up to 0.11 Å [77]. Therefore, we can reasonably assume that the partitioning of Mo to the β-phase reduced the local bond length and overall β-phase lattice parameter. The observed lattice parameter change, however, cannot be converted into the atomic percentage of Mo because the exact spatial distribution of the bond length change in the bcc lattice is unknown.

As the specimens grew tall, all lattice parameters measured on EB-PBF-15 mA and EB-PBF-12.5 mA on the XZ and YZ planes gradually became closer to the lattice parameter of the reference bcc β-phase powder. Further, the quantity of the β-phase increased and the α-phase decreased simultaneously, as shown in Fig. 7(b). Intrinsic annealing by a heated powder bed can cause these phenomena. Because the powder bed for EB-PBF was maintained at a high temperature of 520 °C in this study, the lower part of the specimen experienced a longer annealing time than the top part. A long intrinsic annealing time can enhance the partitioning of Mo to the β-phase. As prolonged intrinsic annealing increased the number of Mo atoms partitioning to the β-phase and reduced its lattice parameter, a larger amount of the alloy was left as the Mo-poor α-phase. The Mo partitioning caused by the intrinsic annealing and the change in the annealing duration along the building direction can explain the shorter lattice parameter of the β-phase at the lower part of the specimen and its gradual increase accompanied by a decrease in the α-phase along the building direction.

4.5. Toward fabrication of residual-stress-free and single bcc β-phase Ti–15Mo–5Zr–3Al

The surface residual stress and β-phase stability analyses of the L-PBF- and EB-PBF-made specimens with different process parameters revealed a stark contrast between the two methods, as summarized in Fig. 11 for the XZ planes of L-PBF-360 W and EB-PBF-15 mA. In L-PBF, a high laser power and high scanning speed caused a greater surface residual stress. The residual stress then disturbed the bcc β-phase stability and induced the bct β-phase. Meanwhile, low laser power and low scanning speed resulted in negligible residual stress and a small amount of lattice distortion. In contrast, in EB-PBF, while no significant residual stress was observed, the intrinsic annealing by the heated powder bed caused partitioning of Mo atoms and transformation of the bcc β-phase to the hexagonal α-phase.

Both the residual stress and phase change are undesirable in the Ti–15Mo–5Zr–3Al alloy. Post-manufacturing heat treatment is often used to reduce the residual stress [17]. However, the analysis results of the EB-PBF-made specimens suggest that such a treatment can cause Mo partitioning and disturb the β-phase stability. The overall comparison of the results in the present study suggests that the low-power and low-scanning-speed L-PBF process has the best potential to produce parts that are free from residual stress and maintain the single-phase state of the bcc β-phase. Achieving desired functionalities requires simultaneous control of the residual stress and phase stability documented in this study and internal microstructures such as equiaxed or highly textured microstructures, which is one of the major challenges in AM because the optimal process window for each does not necessarily matches.

5. Conclusions

This study systematically and quantitatively investigated the difference between L-PBF and EB-PBF methods and their process parameters in surface residual stress and phase stability of the β-phase Ti–15Mo–5Zr–3Al. Specimens fabricated by the L-PBF and EB-PBF methods and different process parameters were analyzed using HP-XRD. The surface residual stress, the stability of the bcc β-phase, and the correlation between the residual stress and deviation from the bcc β-phase were studied. The results are summarized as follows:

(1) While the L-PBF-made specimens exhibited tensile residual stress up to 402 ± 60 MPa in the surface area, the EB-PBF-made specimens showed no significant residual stress.
(2) A comparison of the residual stress measurements and simulated heating and cooling rates for the L-PBF-made specimens suggested that the temperature gradient decreased as the specimen grew, the lower power and scan speed generated lower cooling rates, and the side plane where the beam made U-turns had lower cooling rates than the side plane parallel to the scan direction, all of which contributed to decreased residual stresses.

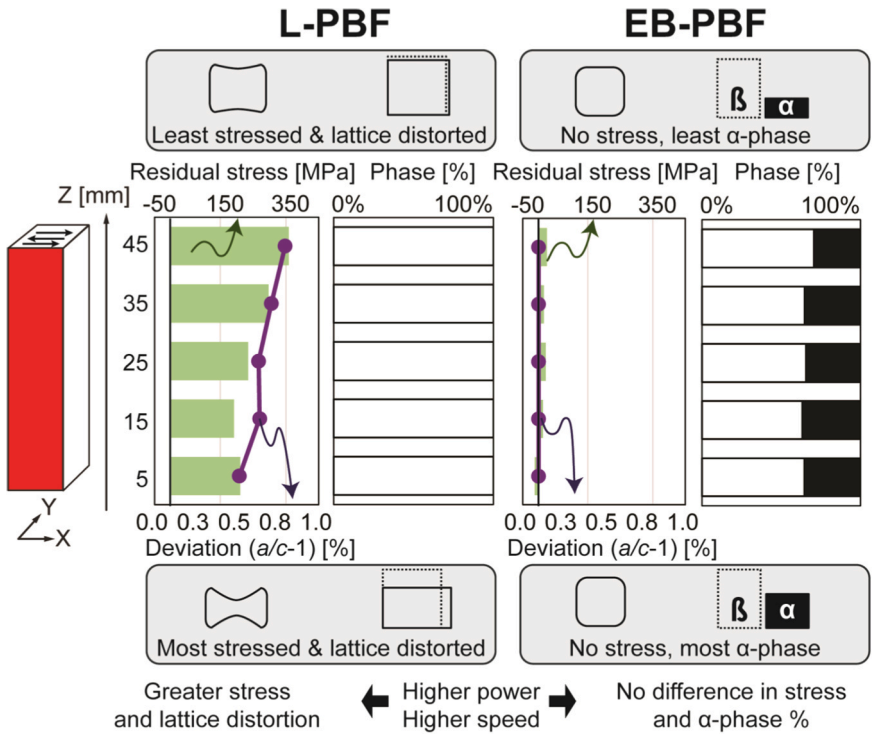

Fig. 11. Comparison of L-PBF and EB-PBF residual stress, lattice distortion, and phase mass% analysis results for the XZ planes of L-PBF-360 W and EB-PBF-15 mA.

(3) In the L-PBF-made specimens, a strong correlation between the residual stress and the deviation from the bcc β structure toward the bct structure was observed, and this correlation illustrated that the residual stress induced a bct β structure.
(4) In the EB-PBF-made specimens, Mo atoms partitioned to the bcc β-phase due to intrinsic annealing; the partitioning decreased the bcc β-phase lattice parameter and increased the amount of α-phase at the same time. The Mo partitioning was more significant in the lower part of the specimens than in the top part because of the longer annealing time.
(5) The observed contrast between the L-PBF-and EB-PBF-made specimens showed that a decreased temperature gradient reduced the residual stress in both cases; however, the bcc β-phase stability was affected differently depending on whether this was achieved by controlling the beam scan conditions or by heating the powder bed.

Lattice distortion, represented by the bct β-phase in this study, can be a precursor to a complete phase transition, which may lead to undesired changes in the physicochemical properties of the material if not intentionally controlled. However, with a comprehensive understanding of how the phase change, residual stresses, fabrication methods, and process parameters relate to each other, an optimized partial phase change can be used to improve the properties of the fabricated parts. This study demonstrated the ability of HP-XRD to analyze the surface residual stress and crystal structures of AM-made metal parts in detail. In this particular example of the β-phase Ti–15Mo–5Zr–3Al, the results provide a new understanding of the different effects of L-PBF and EB-PBF on the residual stress and phase stability. The results suggest that the low-power and low-scanning-speed L-PBF process is more promising than EB-PBF for producing parts that are free from residual stress and maintain the single-phase state of the bcc β-phase.

CRediT authorship contribution statement

Aya Takase: Methodology, Validation, Formal analysis, Investigation, Data Curation, Writing – original draft, Visualization. **Takuya Ishimoto:** Investigation, Writing – review & editing. **Ryoya Suganuma:** Investigation. **Takayoshi Nakano:** Conceptualization, Resources, Writing – review & editing, Supervision, Project administration, Funding acquisition.

Declaration of Competing Interest

The authors declare that they have no known competing financial interests or personal relationships that could have appeared to influence the work reported in this paper.

Acknowledgments

This work was supported by Grants-in-Aid for Scientific Research (JP18H05254) from the Japan Society for the Promotion of Science (JSPS). This work was also partly supported by the Cross-Ministerial Strategic Innovation Promotion Program (SIP), Materials Integration for Revolutionary Design System of Structural Materials, Domain C1: "Development of Additive Manufacturing Process for Ni-based Alloy" from the Japan Science and Technology Agency (JST).

Appendix A. Supporting information

Supplementary data associated with this article can be found in the online version at doi:10.1016/j.addma.2021.102257.

References

[1] A. Sidambe, Biocompatibility of advanced manufactured titanium implants—a review, Materials 7 (2014) 8168–8188, https://doi.org/10.3390/ma7128168.
[2] L.-C. Zhang, H. Attar, Selective laser melting of titanium alloys and titanium matrix composites for biomedical applications: a review, Adv. Eng. Mater. 18 (2016) 463–475, https://doi.org/10.1002/adem.201500419.
[3] P. Li, D.H. Warner, A. Fatemi, N. Phan, Critical assessment of the fatigue performance of additively manufactured Ti–6Al–4V and perspective for future research, Int. J. Fatigue 85 (2016) 130–143, https://doi.org/10.1016/j.ijfatigue.2015.12.003.
[4] M. Schmidt, M. Merklein, D. Bourell, D. Dimitrov, T. Hausotte, K. Wegener, L. Overmeyer, F. Vollertsen, G.N. Levy, Laser based additive manufacturing in

industry and academia, CIRP Ann. 66 (2017) 561–583, https://doi.org/10.1016/j.cirp.2017.05.011.
[5] T. DebRoy, H.L. Wei, J.S. Zuback, T. Mukherjee, J.W. Elmer, J.O. Milewski, A. M. Beese, A. Wilson-Heid, A. De, W. Zhang, Additive manufacturing of metallic components – process, structure and properties, Prog. Mater. Sci. 92 (2018) 112–224, https://doi.org/10.1016/j.pmatsci.2017.10.001.
[6] J. Zhang, X. Wang, S. Paddea, X. Zhang, Fatigue crack propagation behaviour in wire+arc additive manufactured Ti-6Al-4V: effects of microstructure and residual stress, Mater. Des. 90 (2016) 551–561, https://doi.org/10.1016/j.matdes.2015.10.141.
[7] J.-P. Kruth, J. Deckers, E. Yasa, R. Wauthlé, Assessing and comparing influencing factors of residual stresses in selective laser melting using a novel analysis method, Proc. Inst. Mech. Eng. Part B J. Eng. Manufact. 226 (2012) 980–991, https://doi.org/10.1177/0954405412437085.
[8] J. Robinson, I. Ashton, P. Fox, E. Jones, C. Sutcliffe, Determination of the effect of scan strategy on residual stress in laser powder bed fusion additive manufacturing, Addit. Manufact. 23 (2018) 13–24, https://doi.org/10.1016/j.addma.2018.07.001.
[9] E.R. Denlinger, J.C. Heigel, P. Michaleris, T.A. Palmer, Effect of inter-layer dwell time on distortion and residual stress in additive manufacturing of titanium and nickel alloys, J. Mater. Proc. Technol. 215 (2015) 123–131, https://doi.org/10.1016/j.jmatprotec.2014.07.030.
[10] J. Cao, M.A. Gharghouri, P. Nash, Finite-element analysis and experimental validation of thermal residual stress and distortion in electron beam additive manufactured Ti–6Al–4V build plates, J. Mater. Proc. Technol. 237 (2016) 409–419, https://doi.org/10.1016/j.jmatprotec.2016.06.032.
[11] C. Li, Z.Y. Liu, X.Y. Fang, Y.B. Guo, Residual stress in metal additive manufacturing, Procedia CIRP 71 (2018) 348–353, https://doi.org/10.1016/j.procir.2018.05.039.
[12] F. Martina, M.J. Roy, B.A. Szost, S. Terzi, P.A. Colegrove, S.W. Williams, P. J. Withers, J. Meyer, M. Hofmann, Residual stress of as-deposited and rolled wire+arc additive manufacturing Ti–6Al–4V components, Mater. Sci. Technol. 32 (2016) 1439–1448, https://doi.org/10.1080/02670836.2016.1142704.
[13] P. Edwards, M. Ramulu, Fatigue performance evaluation of selective laser melted Ti–6Al–4V, Mater. Sci. Eng. A 598 (2014) 327–337, https://doi.org/10.1016/j.msea.2014.01.041.
[14] J.L. Bartlett, X. Li, An overview of residual stresses in metal powder bed fusion, Addit. Manufact. 27 (2019) 131–149, https://doi.org/10.1016/j.addma.2019.02.020.
[15] D. Novovic, R.C. Dewes, D.K. Aspinwall, W. Voice, P. Bowen, The effect of machined topography and integrity on fatigue life, Int. J. Mach. Tools Manufact. 44 (2004) 125–134, https://doi.org/10.1016/j.ijmachtools.2003.10.018.
[16] J. Günther, D. Krewerth, T. Lippmann, S. Leuders, T. Tröster, A. Weidner, H. Biermann, T. Niendorf, Fatigue life of additively manufactured Ti–6Al–4V in the very high cycle fatigue regime, Int. J. Fatigue 94 (2017) 236–245, https://doi.org/10.1016/j.ijfatigue.2016.05.018.
[17] S. Leuders, M. Thöne, A. Riemer, T. Niendorf, T. Tröster, H.A. Richard, H.J. Maier, On the mechanical behaviour of titanium alloy TiAl6V4 manufactured by selective laser melting: Fatigue resistance and crack growth performance, Int. J. Fatigue 48 (2013) 300–307, https://doi.org/10.1016/j.ijfatigue.2012.11.011.
[18] H. Ali, L. Ma, H. Ghadbeigi, K. Mumtaz, In-situ residual stress reduction, martensitic decomposition and mechanical properties enhancement through high temperature powder bed pre-heating of Selective Laser Melted Ti6Al4V, Mater. Sci. Eng. A 695 (2017) 211–220, https://doi.org/10.1016/j.msea.2017.04.033.
[19] K. Moussaoui, M. Mousseigne, J. Senatore, R. Chieragatti, The effect of roughness and residual stresses on fatigue life time of an alloy of titanium, Int. J. Adv. Manufact. Technol. 78 (2015) 557–563, https://doi.org/10.1007/s00170-014-6596-7.
[20] Y. Liu, S. Li, W. Hou, S. Wang, Y. Hao, R. Yang, T.B. Sercombe, L.-C. Zhang, Electron beam melted beta-type Ti–24Nb–4Zr–8Sn porous structures with high strength-to-modulus ratio, J. Mater. Sci. Technol. 32 (2016) 505–508, https://doi.org/10.1016/j.jmst.2016.03.020.
[21] Y.J. Liu, S.J. Li, H.L. Wang, W.T. Hou, Y.L. Hao, R. Yang, T.B. Sercombe, L. C. Zhang, Microstructure, defects and mechanical behavior of beta-type titanium porous structures manufactured by electron beam melting and selective laser melting, Acta Mater. 113 (2016) 56–67, https://doi.org/10.1016/j.actamat.2016.04.029.
[22] S.-H. Lee, M. Todai, M. Tane, K. Hagihara, H. Nakajima, T. Nakano, Biocompatible low Young's modulus achieved by strong crystallographic elastic anisotropy in Ti–15Mo–5Zr–3Al alloy single crystal, J. Mech. Behav. Biomed. Mater. 14 (2012) 48–54, https://doi.org/10.1016/j.jmbbm.2012.05.005.
[23] M. Tane, K. Hagihara, M. Ueda, T. Nakano, Y. Okuda, Elastic-modulus enhancement during room-temperature aging and its suppression in metastable Ti–Nb-based alloys with low body-centered cubic phase stability, Acta Mater. 102 (2016) 373–384, https://doi.org/10.1016/j.actamat.2015.09.030.
[24] E.S. Fischer, D. Dever, Relation of the of the c′ elastic modulus to stability of b.c.c transition metals, Acta Met. 18 (1970) 265–269, https://doi.org/10.1016/0001-6160(70)90033-7.
[25] H. Gong, K. Rafi, H. Gu, G.D. Janaki Ram, T. Starr, B. Stucker, Influence of defects on mechanical properties of Ti–6Al–4V components produced by selective laser melting and electron beam melting, Mater. Des. 86 (2015) 545–554, https://doi.org/10.1016/j.matdes.2015.07.147.
[26] N.S. Rossini, M. Dassisti, K.Y. Benyounis, A.G. Olabi, Methods of measuring residual stresses in components, Mater. Des. 35 (2012) 572–588, https://doi.org/10.1016/j.matdes.2011.08.022.
[27] T. Rickert, Residual stress measurement by ESPI hole-drilling, Procedia CIRP 45 (2016) 203–206, https://doi.org/10.1016/j.procir.2016.02.256.
[28] SAE_HS-784 Residual Stress Measurement by X-Ray Diffraction_2003 Edition, (2003).
[29] A.S. Wu, D.W. Brown, M. Kumar, G.F. Gallegos, W.E. King, An experimental investigation into additive manufacturing-induced residual stresses in 316L stainless steel, Metal. Mater. Trans. A. 45 (2014) 6260–6270, https://doi.org/10.1007/s11661-014-2549-x.
[30] T. Watkins, Neutron characterization for additive manufacturing, Adv. Mater. Process. (2013) 23–27.
[31] D.W. Brown, J.D. Bernardin, J.S. Carpenter, B. Clausen, D. Spernjak, J. M. Thompson, Neutron diffraction measurements of residual stress in additively manufactured stainless steel, Mater. Sci. Eng. A 678 (2016) 291–298, https://doi.org/10.1016/j.msea.2016.09.086.
[32] Measurement of residual stress in materials using neutrons, Proceedings of a technical meeting, 2003, International Atomic Energy Agency, Vienna, 2005. ⟨http://www-pub.iaea.org/MTCD/publications/PDF/te_1457_web.pdf⟩ Accessed 20 August 2021., (n.d.).
[33] C. Xu, W. Song, Q. Pan, H. Li, S. Liu, Nondestructive testing residual stress using ultrasonic critical refracted longitudinal wave, Phys. Proc. 70 (2015) 594–598, https://doi.org/10.1016/j.phpro.2015.08.030.
[34] L.M. Sochalski-Kolbus, E.A. Payzant, P.A. Cornwell, T.R. Watkins, S.S. Babu, R. R. Dehoff, M. Lorenz, O. Ovchinnikova, C. Duty, Comparison of residual stresses in inconel 718 simple parts made by electron beam melting and direct laser metal sintering, Metal. Mater. Trans. A 46 (2015) 1419–1432, https://doi.org/10.1007/s11661-014-2722-2.
[35] Z. Wang, E. Denlinger, P. Michaleris, A.D. Stoica, D. Ma, A.M. Beese, Residual stress mapping in Inconel 625 fabricated through additive manufacturing: method for neutron diffraction measurements to validate thermomechanical model predictions, Mater. Des. 113 (2017) 169–177, https://doi.org/10.1016/j.matdes.2016.10.003.
[36] R. Erni, M.D. Rossell, C. Kisielowski, U. Dahmen, Atomic-resolution imaging with a sub-50-pm electron probe, Phys. Rev. Lett. 102 (2009), 096101, https://doi.org/10.1103/PhysRevLett.102.096101.
[37] T. Mitsunaga, M. Saigo, G. Fujinawa, High-precision parallel-beam X-ray system for high-temperature diffraction studies, Powder Diffr. 17 (2002) 173–177.
[38] A. Takase, Effect of systematic errors on lattice parameter refinement, 60th Annual Conference on Applications of X-Ray Analysis. (2011) D-81.
[39] T. Takashima, Y. Koizumi, Y. Li, K. Yamanaka, T. Saito, A. Chiba, Effect of building position on phase distribution in Co–Cr–Mo alloy additive manufactured by electron-beam melting, Mater. Trans. 57 (2016) 2041–2047, https://doi.org/10.2320/matertrans.Y-M2016826.
[40] T. Ishimoto, K. Hagihara, K. Hisamoto, S.-H. Sun, T. Nakano, Crystallographic texture control of beta-type Ti–15Mo–5Zr–3Al alloy by selective laser melting for the development of novel implants with a biocompatible low Young's modulus, Scr. Mater. 132 (2017) 34–38, https://doi.org/10.1016/j.scriptamat.2016.12.038.
[41] S.-H. Sun, T. Ishimoto, K. Hagihara, Y. Tsutsumi, T. Hanawa, T. Nakano, Excellent mechanical and corrosion properties of austenitic stainless steel with a unique crystallographic lamellar microstructure via selective laser melting, Scr. Mater. 159 (2019) 89–93, https://doi.org/10.1016/j.scriptamat.2018.09.017.
[42] Standard Test Method for Verifying the Alignment of X-Ray Diffraction Instrumentation for Residual Stress Measurement - Designation: E 915 – 96 (Reapproved 2002), ASTM International. (2002).
[43] G.S. Pawley, Unit-cell refinement from powder diffraction scans, J. Appl. Crystallogr. 14 (1981) 357–361, https://doi.org/10.1107/S0021889881009618.
[44] Q. Chen, X. Liang, D. Hayduke, J. Liu, L. Cheng, J. Oskin, R. Whitmore, A.C. To, An inherent strain based multiscale modeling framework for simulating part-scale residual deformation for direct metal laser sintering, Addit. Manuf. 28 (2019) 406–418, https://doi.org/10.1016/j.addma.2019.05.021.
[45] D.L. Bish, S.A. Howard, Quantitative phase analysis using the Rietveld method, J. Appl. Crystallogr. 21 (1988) 86–91, https://doi.org/10.1107/S0021889887009415.
[46] John A. Small, Robert L. Watters, Jr., Certificate SRM 660c - Line Position and Line Shape Standard for Powder Diffraction (Lanthanum Hexaboride Powder), (2015). ⟨https://www-s.nist.gov/srmors/view_cert.cfm?srm=660C⟩. Accessed 20 August 2021., (n.d.).
[47] J.I. Langford, Some applications of pattern fitting to powder diffraction data, Prog. Cryst. Growth Charact. 14 (1987) 185–211, https://doi.org/10.1016/0146-3535(87)90018-9.
[48] H.J. Willy, X. Li, Z. Chen, T.S. Herng, S. Chang, C.Y.A. Ong, C. Li, J. Ding, Model of laser energy absorption adjusted to optical measurements with effective use in finite element simulation of selective laser melting, Mater. Des. 157 (2018) 24–34, https://doi.org/10.1016/j.matdes.2018.07.029.
[49] G.L. Knapp, N. Raghavan, A. Plotkowski, T. DebRoy, Experiments and simulations on solidification microstructure for Inconel 718 in powder bed fusion electron beam additive manufacturing, Addit. Manufact. 25 (2019) 511–521, https://doi.org/10.1016/j.addma.2018.12.001.
[50] S. Liu, H. Zhu, G. Peng, J. Yin, X. Zeng, Microstructure prediction of selective laser melting AlSi10Mg using finite element analysis, Mater. Des. 142 (2018) 319–328, https://doi.org/10.1016/j.matdes.2018.01.022.
[51] Q. Chen, X. Liang, D. Hayduke, J. Liu, L. Cheng, J. Oskin, R. Whitmore, A.C. To, An inherent strain based multiscale modeling framework for simulating part-scale residual deformation for direct metal laser sintering, Addit. Manufact. 28 (2019) 406–418, https://doi.org/10.1016/j.addma.2019.05.021.

[52] EOS M 290 – industrial 3D printed parts from metal materials. ⟨https://www.eos.info/en/additive-manufacturing/3d-printing-metal/eos-metal-systems/eos-m-290⟩. Accessed 20 August 2021., (n.d.).
[53] A. Foroozmehr, M. Badrossamay, E. Foroozmehr, S. Golabi, Finite element simulation of selective laser melting process considering optical penetration depth of laser in powder bed, Mater. Des. 89 (2016) 255–263, https://doi.org/10.1016/j.matdes.2015.10.002.
[54] M.-S. Pham, B. Dovgyy, P.A. Hooper, C.M. Gourlay, A. Piglione, The role of side-branching in microstructure development in laser powder-bed fusion, Nat. Commun. 11 (2020) 749, https://doi.org/10.1038/s41467-020-14453-3.
[55] H.S. Carslaw, J.C. Jaeger. Conduction of Heat in Solids, 2nd ed., Oxford University Press, Oxford, 1986.
[56] Y. Li, D. Gu, Parametric analysis of thermal behavior during selective laser melting additive manufacturing of aluminum alloy powder, Mater. Des. 63 (2014) 856–867, https://doi.org/10.1016/j.matdes.2014.07.006.
[57] S.J. Wolff, S. Lin, E.J. Faierson, W.K. Liu, G.J. Wagner, J. Cao, A framework to link localized cooling and properties of directed energy deposition (DED)-processed Ti–6Al–4V, Acta Mater. 132 (2017) 106–117, https://doi.org/10.1016/j.actamat.2017.04.027.
[58] V. Pashkis, V. Pashkis: Trans. AFS, 53 (1945), 90., Trans. AFS. 53 (1945) 90.
[59] ⟨https://www.azom.com/article.aspx?ArticleID=9427⟩ Accessed 20 August 2021., (n.d.).
[60] M. Dallago, V. Fontanari, E. Torresani, M. Leoni, C. Pederzolli, C. Potrich, M. Benedetti, Fatigue and biological properties of Ti–6Al–4V ELI cellular structures with variously arranged cubic cells made by selective laser melting, J. Mech. Behav. Biomed. Mater. 78 (2018) 381–394, https://doi.org/10.1016/j.jmbbm.2017.11.044.
[61] M.A. Surmeneva, R.A. Surmenev, E.A. Chudinova, A. Koptioug, M.S. Tkachev, S. N. Gorodzha, L.-E. Rännar, Fabrication of multiple-layered gradient cellular metal scaffold via electron beam melting for segmental bone reconstruction, Mater. Des. 133 (2017) 195–204, https://doi.org/10.1016/j.matdes.2017.07.059.
[62] H. Galarraga, R.J. Warren, D.A. Lados, R.R. Dehoff, M.M. Kirka, P. Nandwana, Effects of heat treatments on microstructure and properties of Ti–6Al–4V ELI alloy fabricated by electron beam melting (EBM), Mater. Sci. Eng. A. 685 (2017) 417–428, https://doi.org/10.1016/j.msea.2017.01.019.
[63] B.D. Cullity. Elements of x-Ray Diffraction, 2d ed., Addison-Wesley Pub. Co, Reading, Mass, 1978.
[64] A. Takase, T. Ishimoto, R. Suganuma, T. Nakano, Lattice distortion in selective laser melting (SLM)-manufactured unstable β-type Ti–15Mo–5Zr–3Al alloy analyzed by high-precision X-ray diffractometry, Scr. Mater. 201 (2021), 113953, https://doi.org/10.1016/j.scriptamat.2021.113953.
[65] P.J. Potts, A Handbook of Silicate Rock Analysis, (1987) p. 336. https://doi.org/10.1007/978–94-015–3988-3.
[66] A. Brostrøm, K. Kling, K. Hougaard, K. Mølhave, Analysis of electron transparent beam-sensitive samples using scanning electron microscopy coupled with energy-dispersive X-ray spectroscopy, Microsc. Microanal. 26 (2020) 373–386, https://doi.org/10.1017/S1431927620001464.
[67] H.E. Höfer, G.P. Brey, The iron oxidation state of garnet by electron microprobe: its determination with the flank method combined with major-element analysis, Am. Min. 92 (2007) 873–885, https://doi.org/10.2138/am.2007.2390.
[68] T. Mishurova, K. Artzt, J. Haubrich, G. Requena, G. Bruno, Exploring the correlation between subsurface residual stresses and manufacturing parameters in laser powder bed fused Ti–6Al–4V, Metals 9 (2019) 261, https://doi.org/10.3390/met9020261.
[69] C.H. Fu, Y.B. Guo, Three-dimensional temperature gradient mechanism in selective laser melting of Ti–6Al–4V, J. Manuf. Sci. Eng. 136 (2014), 061004, https://doi.org/10.1115/1.4028539.
[70] J. Reijonen, A. Revuelta, T. Riipinen, K. Ruusuvuori, P. Puukko, On the effect of shielding gas flow on porosity and melt pool geometry in laser powder bed fusion additive manufacturing, Addit. Manuf. 32 (2020), 101030, https://doi.org/10.1016/j.addma.2019.101030.
[71] L. Mugwagwa, D. Dimitrov, S. Matope, I. Yadroitsev, Influence of process parameters on residual stress related distortions in selective laser melting, Procedia Manuf. 21 (2018) 92–99, https://doi.org/10.1016/j.promfg.2018.02.099.
[72] T. Mukherjee, V. Manvatkar, A. De, T. DebRoy, Mitigation of thermal distortion during additive manufacturing, Scr. Mater. 127 (2017) 79–83, https://doi.org/10.1016/j.scriptamat.2016.09.001.
[73] I. Yadroitsev, P. Krakhmalev, I. Yadroitsava, Selective laser melting of Ti6Al4V alloy for biomedical applications: temperature monitoring and microstructural evolution, J. Alloy. Compd. 583 (2014) 404–409, https://doi.org/10.1016/j.jallcom.2013.08.183.
[74] L.A. Bendersky, A. Roytburd, W.J. Boettinger, Phase transformations in the (Ti, Al) 3 Nb section of the Ti–Al–Nb system—I. Microstructural predictions based on a subgroup relation between phases, Acta Metall. Mater. 42 (1994) 2323–2335, https://doi.org/10.1016/0956-7151(94)90311-5.
[75] T. Inamura, H. Hosoda, K. Wakashima, S. Miyazaki, Anisotropy and temperature dependence of Young's modulus in textured tinbal biomedical shape memory alloy, Mater. Trans. 46 (2005) 1597–1603, https://doi.org/10.2320/matertrans.46.1597.
[76] L.L. Chang, Y.D. Wang, Y. Ren, In-situ investigation of stress-induced martensitic transformation in Ti–Nb binary alloys with low Young's modulus, Mater. Sci. Eng. A 651 (2016) 442–448, https://doi.org/10.1016/j.msea.2015.11.005.
[77] L.-F. Huang, B. Grabowski, J. Zhang, M.-J. Lai, C.C. Tasan, S. Sandlöbes, D. Raabe, J. Neugebauer, From electronic structure to phase diagrams: a bottom-up approach to understand the stability of titanium–transition metal alloys, Acta Mater. 113 (2016) 311–319, https://doi.org/10.1016/j.actamat.2016.04.059.